Experimental Investigations of Strain Localization in Concrete using Digital Image Correlation (DIC) Technique

Jan Kozicki, Jacek Tejchman

Faculty of Civil and Environmental Engineering, Gdańsk University of Technology,
Gdańsk-Wrzeszcz, ul. Narutowicza 11/12, e-mails: jkozicki@pg.gda.pl, tejchmk@pg.gda.pl

Abstract

The paper presents results of experimental investigations of strain localization in concrete using a non-destructive method called Digital Image Correlation (DIC) technique. This technique measures surface displacements from digital images. The model tests were carried out with notched concrete specimens under three-point bending. Three different beam sizes and two different concrete mixes were used. During experiments, load–deflection curves and evolution of fracture process zone were determined. The measured size effect in strength was compared with the deterministic size effect law by Bazant (1984) and experimental results by Le Bellégo et al (2003).

Key words: concrete beams, digital image correlation, fracture process zone, strain localization, three-point bending

1. Introduction

Strain localization in the form of fracture process zones (FPZ) is a fundamental phenomenon in such quasi-brittle materials as concrete (van Vliet, van Mier 1996, Bazant, Planas 1998, Bazant 2003). The determination of the width and spacing of strain localization is crucial to evaluate the material strength at peak and in the post-peak regime. To describe strain localization properly (width and spacing), continuum constitutive models should include a characteristic length of micro-structure (Bazant 2003). The characteristic length in brittle materials is usually related to the aggregate size. According to Pijauder-Cabot and Bazant (1987) and Bazant and Oh (1983), it is approximately $3 \times d_a$, where d_a is the maximum aggregate size. It is usually determined with an inverse identification process of experiment (Geers et al 1996, Mahnken, Kuhl 1999) since it cannot be measured directly. Recently Le Bellégo et al (2003) presented a calibration method of non-local models containing a characteristic length on the basis of three size effect bending tests. However, such a method is not consistent (Bobiński, Tejchman 2006). The determination of one representative characteristic length of micro-structure is very complex in concrete

since strain localization can include a mixed mode (cracks and shear zones (Bazant, Jirasek 2002)). A characteristic length is a one-dimensional quantity, but is related to the fracture process zone with a certain area or volume (Bazant, Jirasek 2002) which increases during deformation (demonstrated, e.g., by acoustic emission measurements by Pijauder-Cabot et al (2004)). In turn, other researchers conclude that the characteristic length is not a constant, and depends on the type of the boundary value problem and the current level of damage (Ferrara, di Prisco 2001). The only way to determine the characteristic length are simultaneous measurements of load–displacement curves and widths of the fracture process zones in experiments carried out with the same concrete for different boundary value problems and specimen sizes (Bobiński, Tejchman 2006).

The intention of the paper is to show the capability of a non-invasive method called Digital Image Correlation technique (Bhandari, Inoue 2005) (called also Particle Image Velocimetry PIV) to measure directly surface displacements in model concrete beams subject to three-point bending. The technique which was originally developed in the field of experimental fluid and gas mechanics (Raffel et al 1998) has nowadays been frequently used in granular materials (Nübel 2002, White et al 2003, Michalowski, Shi 2003, Eckert et al 2003, Rechenmacher 2006, Słomiński et al 2006, Słomiński et al 2007). The deformation quantities are, however, significantly larger than those in brittle materials.

The model tests were carried out with notched concrete specimens subject to three-point bending. Three different beam sizes and two different concrete mixes were used. During experiments, load–deflection curves and evolution of fracture process zone were determined. The measured size effect results were compared with the size effect law by Bazant (1984) and experimental results by Le Bellégo et al (2003).

The present paper is organized as follows. In Section 2, the DIC technique is described in detail. Section 3 discusses the accuracy of the method. The information about the experimental setup is given in Section 4. The experimental results are presented in Section 5. Finally, some conclusions are given in Section 6.

To use DIC, the software written in C++ by the first author was applied.

2. Digital Image Correlation Technique

DIC is a powerful optical surface velocity-measuring tool to visualize two dimensional deformations. The coloured surface serves as tracers. A high resolution monitoring of different deformations can be obtained by processing successive digital images taken with a constant time between frames from a normal digital camera. Owing to that, strain localization can be visualized and analyzed in detail. Digital camera sensors are comprised of tiny, light-sensitive elements called pixels. When an image is captured, each pixel reflects three numbers (called the colour components $YCbCr$) in proportion to the amount of light reflected from the imaged object,
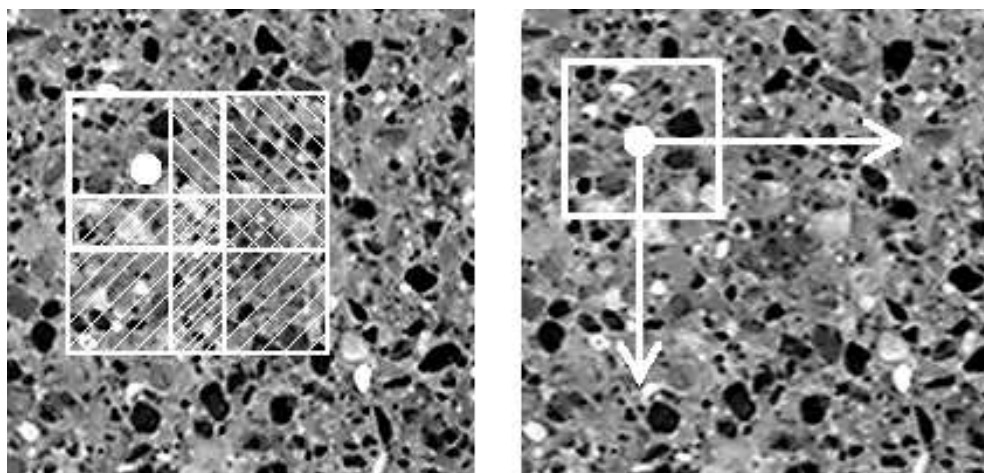
Fig. 1. DIC analysis: two digital images with the marked search patch (white square) and other overlapping search patches (hashed squares). To calculate the correlation, the search patch is moved 'pixel by pixel' through the second image (right picture)

where Y is the luminosity (brightness), C_b is the blueness and C_r is the redness. The DIC system interprets differences in light intensity as a gray-scale pattern recorded at each pixel on CCD-camera (Charge Coupled Device). Three functions are of major importance for DIC: image field intensity, cross-correlation function and interpolation function. The image intensity field assigns to each point in the image plane a scalar value which reflects the light intensity (Y-colour component) of the corresponding point in the physical space. The gray levels range numerically between 0 (black) and 255 (white) for an 8-bit image. A so-called area of interest (AOI) is cut out of the digital image and small overlapping sub-areas called search patches (White et al 2003) are chosen (Fig. 1). The search patch ranges in size from 15×15 pixels up to 240×240 pixels. If the deformation between two images is sufficiently small, the patterns of the interrogation cells are supposed not to change their characteristics (only their locations). A deformation pattern is detected by comparing two consecutive images captured by a camera which remains in a fixed position with its axis oriented perpendicular to the plane of deformation. To find a local displacement between images 1 and 2, a search zone is extracted from the second image. A correct local displacement vector for each interrogation cell is accomplished by means of a cross-correlation function between two consecutive brightness distributions (Y color component) in two digital images. The function calculates simply possible displacements by correlating all gray values from the first image with all gray values from the second image. The correlation plane is evaluated at single pixel intervals, this means that the resolution is equal to one pixel. By fitting an interpolation function to the region close to the peak, the displacement vector is established with a high accuracy (equal to the correlation offset). The peak

in the correlation function indicates that the two images overlay each other (thus, it indicates the "degree of match" between two images).

The first step in the image preprocessing is to convert the usual colour space RGB into the YC_bC_r colour space (ISO/TC42N 4378 TIFF/EP). To calculate a strain field on the specimen surface, two successive digital images have to be compared with each other. First, one pixel is selected on the first digital image, then a square search patch of a certain size is chosen around it. Next, a search for this patch on the second image is done by using a correlation function (Fig. 1). Two different correlation functions were compared: first using the Spearman rank correlation coefficient R_1 (Bhandari, Inoue 2005) and the Pearson's product–moment correlation coefficient R_2. The first method is faster but less stable during calculations with large sizes of the search patch:

$$R_1(x,y) = \frac{(\sum x_i y_i)^2}{\sum x_i^2 \sum y_i^2}. \tag{1}$$

The parameters x and y refer to the first and second image, respectively and i stands for the number of the pixel. In turn, the Pearson's product–moment correlation method produces numerically more stable results, although it needs more time (ca. 20% more) for calculations. It is obtained by dividing the covariance of two variables by the product of their standard deviations (n – number of pixels in the search patch):

$$R_2(x,y) = \frac{n \sum x_i y_i - \sum x_i \sum y_i}{\sqrt{n \sum x_i^2 - (\sum x_i)^2} \; \sqrt{n \sum y_i^2 - (\sum y_i)^2}}. \tag{2}$$

Figure 2 shows a comparison between two different correlation functions and search patch sizes. The Pearson method with the size of 200 pixels has the smallest amount of noise, but also a less steep peak. A too small search patch produces noise. In turn, the Spearman method generates too small a correlation peak with respect to the correlation plane. An alternative to both methods is the application of a FFT convolution approach (which is faster than the two above mentioned methods).

The top of the correlation peak is usually not clearly distinguished, as the correlation function generates the results for each pixel of the image. To determine the top of the peak, a sub-pixel interpolation has to be performed. Figure 3a, b shows a correlation plane used for interpolating the correlation peak for two different interpolation functions (Dersch 1999). The first one was the spline36 interpolation (Fig. 4) which used a 6×6 pixel image area (Fig. 3b) to calculate the interpolated value:
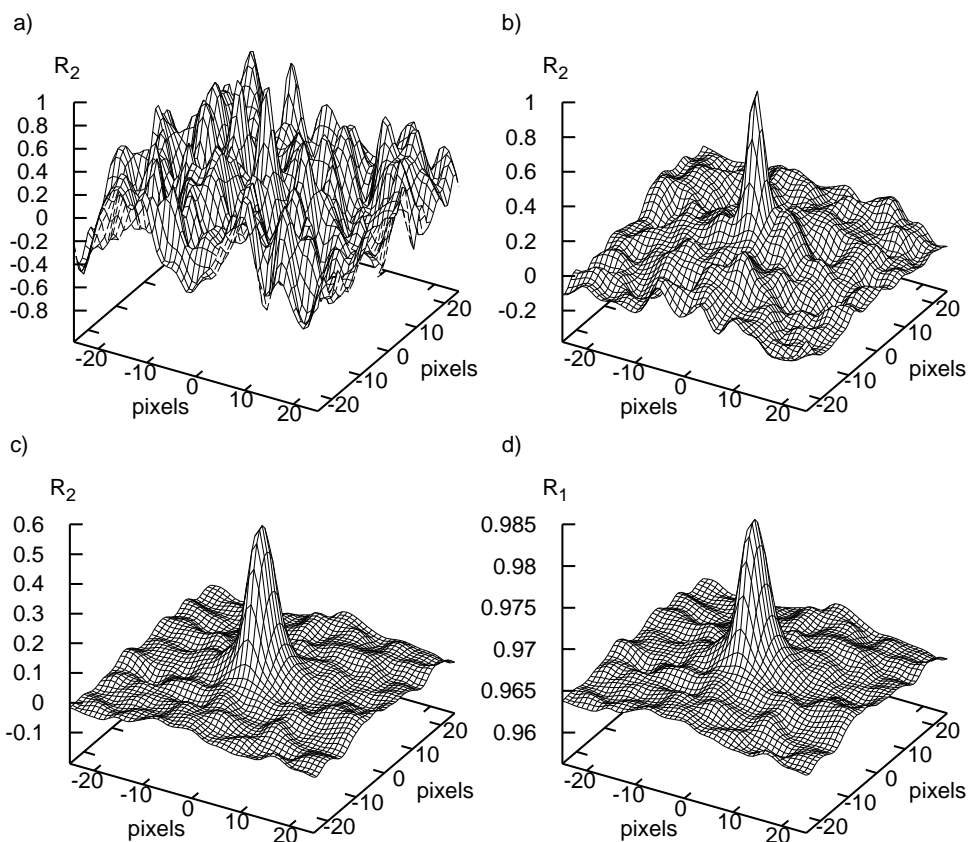
Fig. 2. Comparison between the correlation functions and search patch sizes: a) 10 pixels, Pearson's formula (Eq. 2), b) 50 pixels, Pearson's formula (Eq. 2), c) 200 pixels, Pearson's formula (Eq. 2), d) 200 pixels, Spearman's formula (Eq. 1)

$$w_1(a) = \begin{cases} \left[\left(\frac{13}{11}a - \frac{453}{209}\right)a - \frac{3}{209}\right]a + 1 & \text{for } 0 < a < 1, \\[2mm] \left[\left(-\frac{6}{11}(a-1) + \frac{270}{209}\right)(a-1) - \frac{156}{209}\right](a-1) & \text{for } 1 < a < 2, \\[2mm] \left[\left(\frac{1}{11}(a-2) - \frac{45}{209}\right)(a-2) + \frac{26}{209}\right](a-2) & \text{for } 2 < a < 3. \end{cases} \quad (3)$$

The second interpolation function was sinc256 (Figs. 3a and 4) which used a 16×16 pixel image area:
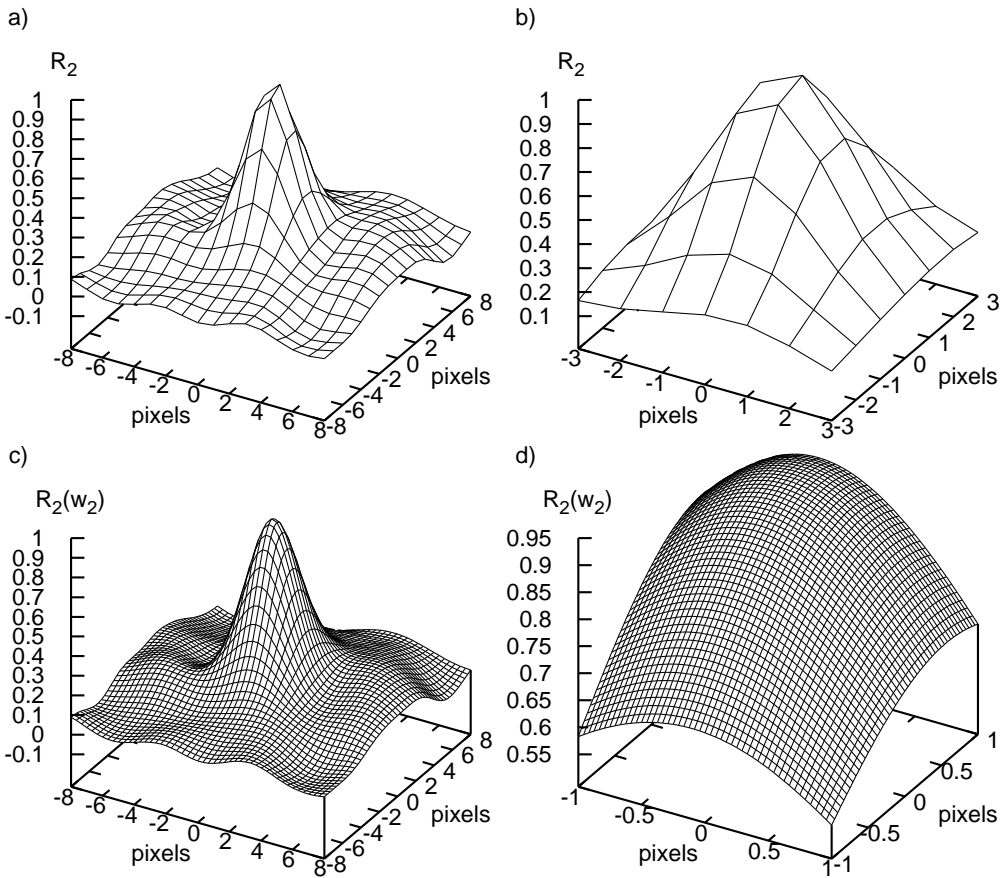
Fig. 3. Correlation plane with correlation peak: a) 16×16 pixel area used in interpolation by sinc256, b) 6×6 pixel area used in interpolation by spline36, c) surface after sub–pixel interpolation, d) zoom on the peak after sub–pixel interpolation

$$
w_2(a) = \begin{cases} 1 & \text{for } a = 0 \\[2mm] \dfrac{\sin(\pi a)}{\pi a} \cdot \dfrac{\sin\left(\dfrac{\pi a}{8}\right)}{\dfrac{\pi a}{8}} & \text{for } a > 0 \end{cases} \quad . \tag{4}
$$

This interpolation was slower (by ca. 10%) than the first one. Generally, the interpolation was evaluated at 1/500th pixel intervals, yielding a system resolution of 0.002 pixels (Fig. 3c, d). Figure 5 shows the difference between the obtained results of strain fields with and without sub–pixel interpolation. The results demonstrate that the application of a sub–pixel interpolation increases the accuracy of calculations.

a)   b)
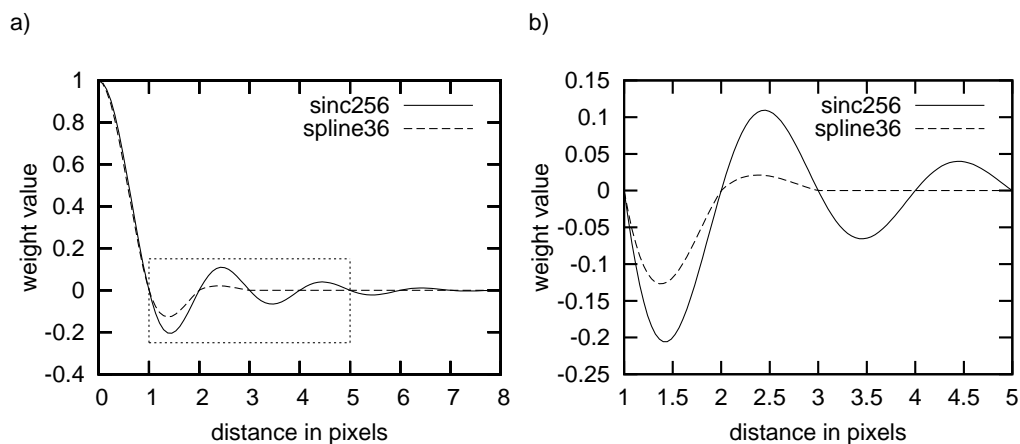
Fig. 4. Interpolation functions used to achieve a sub–pixel precision

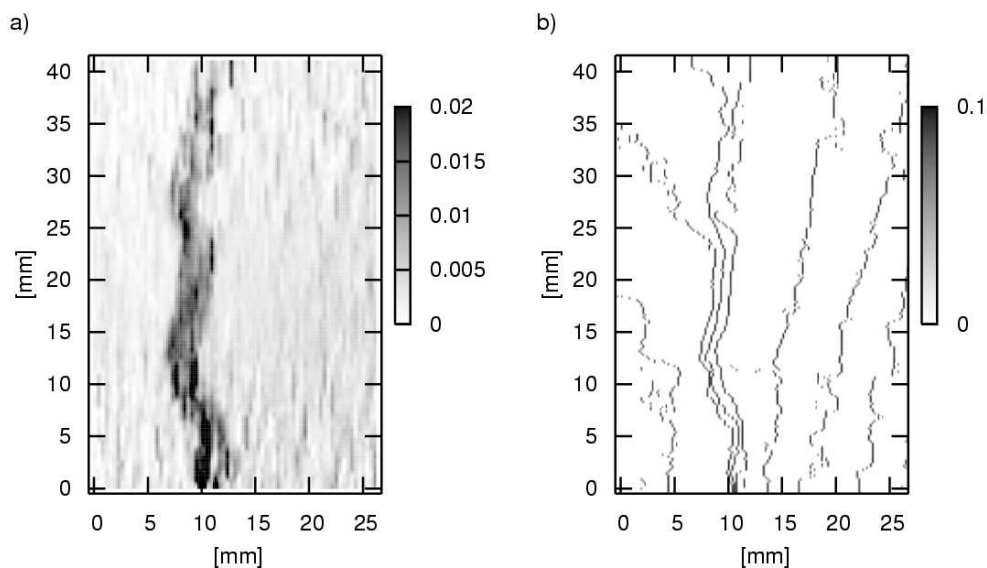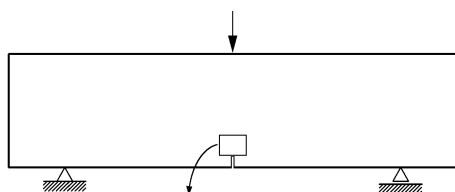a)   b)

Fig. 5. Effect of sub–pixel interpolation on precision of horizontal strain on concrete surface above the notch: a) with sub–pixel interpolation, b) without sub–pixel interpolation

3. Precision of DIC Measurements

A series of initial experiments was conducted to assess the precision of DIC (according to the procedure proposed by White et al (2003)). Figure 6 shows the standard deviation of the measured strain vs. the assumed strain against the search patch size for two different correlation and interpolation functions. For this purpose, two successive digital images of the concrete specimen were compared wherein the resulting strain was zero. The most accurate results were obtained with Pearson's method used in combination with the interpolation function sinc256. Therefore, all further calculations were performed using only this method.
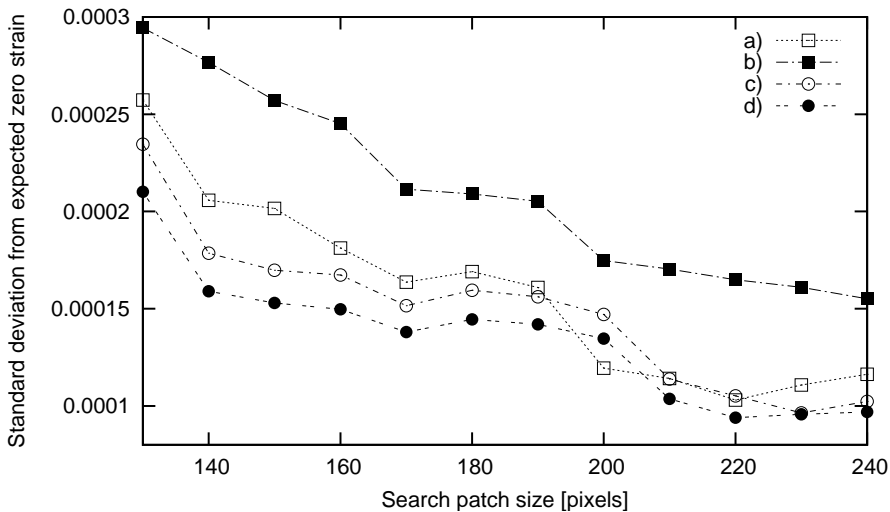
Fig. 6. Effect of two correlation and two interpolation functions on the standard deviation: a) Spearman's method with spline36 interpolation, b) Spearman's method with sinc256 interpolation, c) Pearson's method with spline36 interpolation, d) Pearson's method with sinc256 interpolation

Figures 7–9 show the results for the following digital image pairs:
a) two subsequent images of the concrete specimen,
b) random image with 3×3 "grains",
c) single image of the concrete specimen compared with itself,
d) random image with 1×1 "grains".

For all four cases, Fig. 8 shows that the DIC precision is better than 0.0005 for the search patches larger than 60 pixels.

The precision errors are associated with the asymmetry of the correlation peak. In the case of the random image with 1×1 pixel "grains", an almost perfect match was found (Fig. 8d) with the highest precision. For 3×3 pixel "grains" and two subsequent images (Fig. 8a, b) no perfect match was found, since the correlation
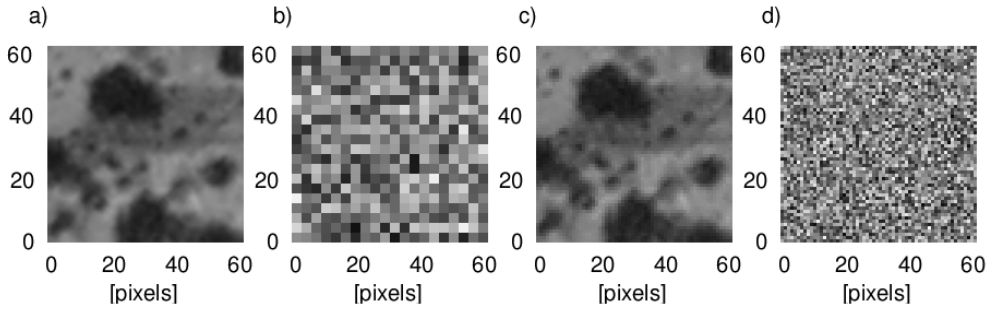
Fig. 7. Images used in validation experiments: a) two subsequent images, b) random image with 3×3 "grains", c) single image, d) random image with 1×1 "grains"
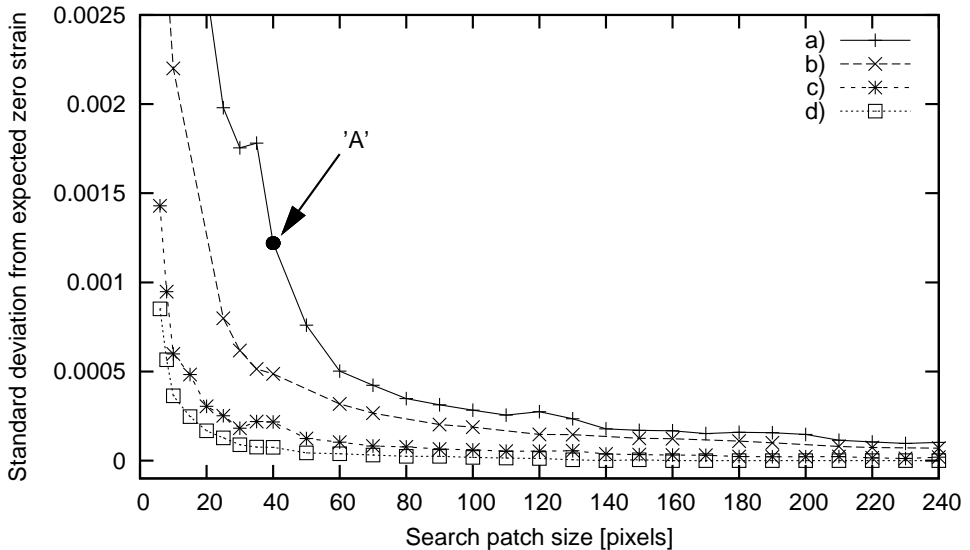

Fig. 8. DIC precision against the search patch size (for strain equal to zero): a) two subsequent images, b) random image with 3×3 "grains", c) single image, d) random image with 1×1 "grains"
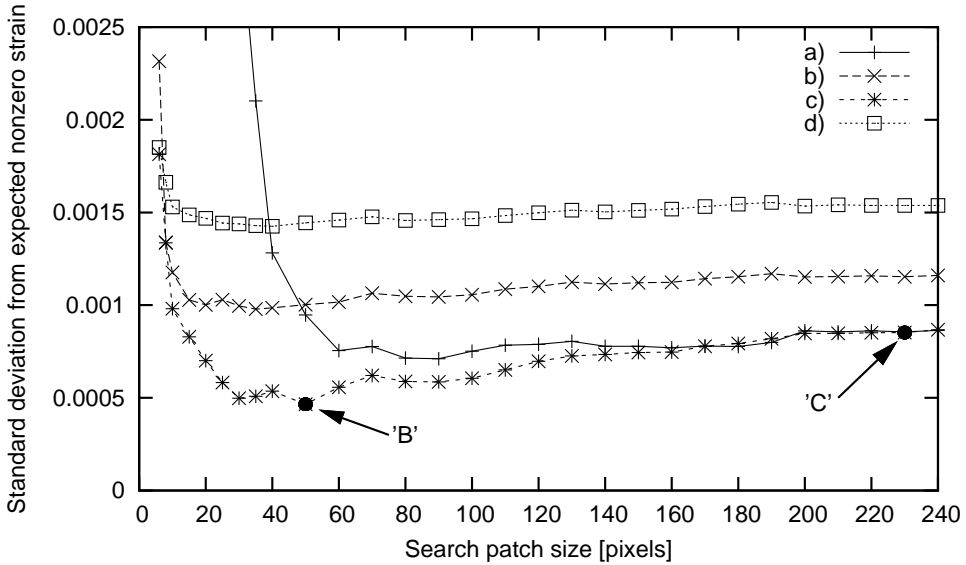
Fig. 9. DIC precision against the search patch size for strain oscillating between 0 and 0.0033 every 300 pixels
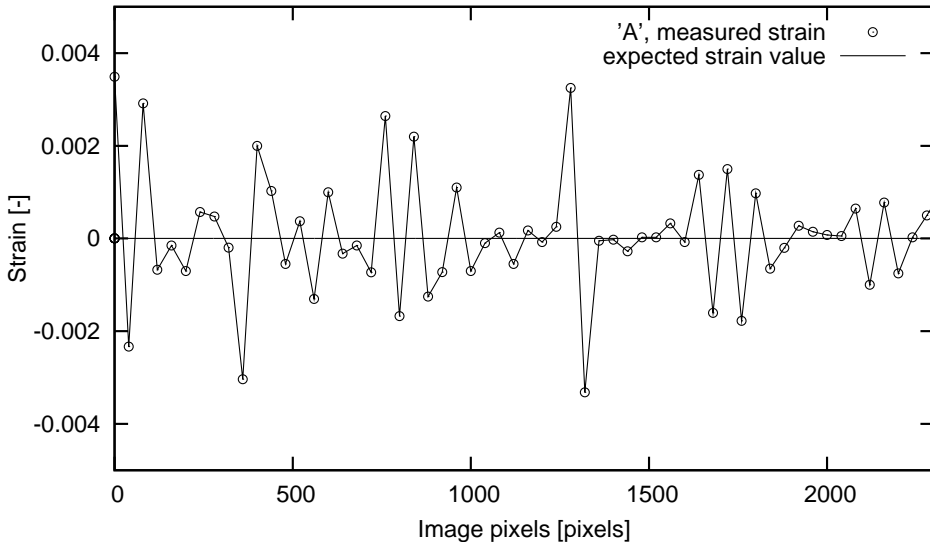

Fig. 10. Strain along a single line of the image for the point 'A' of Fig. 8 (search patch size is 40 pixels, standard deviation from expected zero strain is 0.0012)

peak was asymmetric. Strain value fluctuation along a single line of the image is shown on Fig. 10 for the point 'A' of Fig. 8.
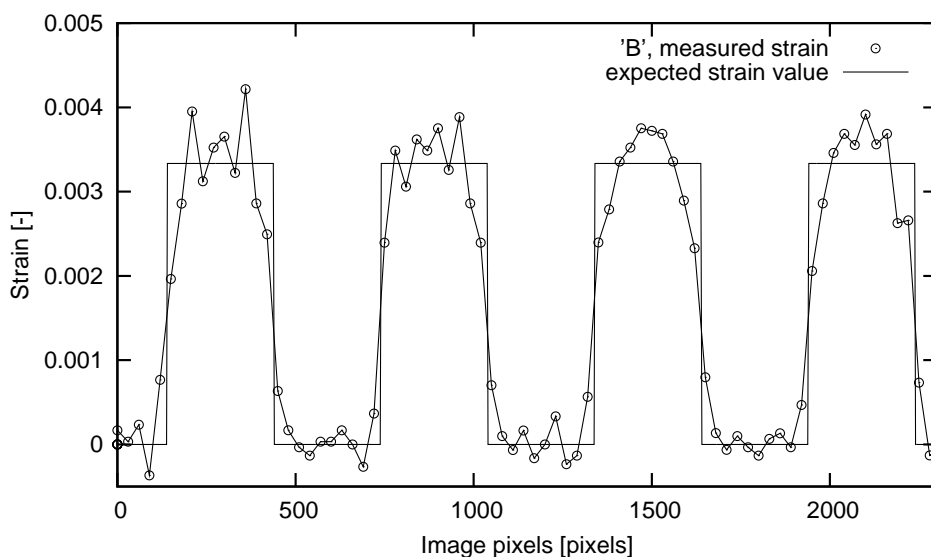
Fig. 11. Strain along a single line of the image for the point 'B' of Fig. 9 (search patch size is 50 pixels, width of the zone of strain localization is estimated with high precision, standard deviation from expected strain is 0.0005)

Next, the second image for all four cases (Fig. 7) was artificially modified, so that strain oscillated between 0 and 0.0033 every 300 pixels. Figure 9 reveals a higher precision for the real case (Fig. 7a, c) than for the random pixel pattern (Fig. 7b, d). In the randomly generated pixel pattern, the noise has high amplitude in the frequency domain. Thus, by stretching it (to achieve strain 0.0033), an image interference occurs. The real images have a small amplitude in the frequency domain. In this way, no artefacts are generated. Moreover, a large search patch size blurs the boundaries between oscillating strain values while a smaller search patch size (but not too small) yields more accurate results. Figures 11 and 12 clearly show this result for points 'B' and 'C' of Fig. 9. The precision of DIC strongly depends on the search patch size and the quality of a random pattern in the image. It is recommended that the pattern dots on the concrete surface should include 4–10 pixels on the captured image. Thus, in this case, no image interference takes place.

The selection of an optimum search patch size in the DIC analysis requires two conflicting parameters to be balanced. The larger search patch offers an improved accuracy (Fig. 8), but it blurs the boundary between strain values (Fig. 12). The number of measurement points depends only on the computational time, since the distance between the search patch centres can be as small as one pixel. In the calculations presented here, this distance was assumed to lie between 10 and 40 pixels. Hence it was small enough to not influence the resolution of results.
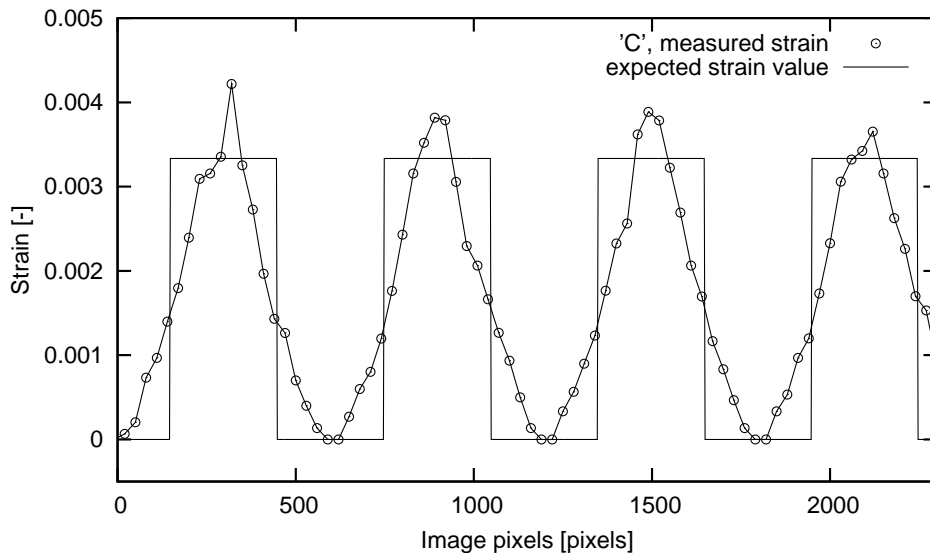
Fig. 12. Strain along a single line of the image for the point 'C' of Fig. 9 (search patch size is 230 pixels, boundaries of zone of strain localization are blurred, standard deviation from expected strain is 0.0009)

4. Experimental Setup

The model tests were performed with 12 notched concrete beams of different sizes under three-point bending (with free ends). Figure 13 shows the geometry of three concrete beam specimens with the thickness of 40 mm (the same geometry was assumed in laboratory experiments by Le Bellégo et al (2003). The beam heights D were 80 mm (small size beam), 160 mm (medium size specimen) and 320 mm (large size beam), respectively. A notch of the depth $D/10$ and thickness of 3 mm was placed in the middle of each beam bottom. The deformation in the beams was induced by a vertical displacement prescribed at the mid-span with a rate of 0.01 mm/min. The entire experiment with a single beam lasted approximately one hour.

The specimens were prepared using two different mixes (Tab. 1) consisting of ordinary Portland cement, water and sand (mean aggregate diameter $d_{50} = 0.5$ mm) or gravel (mean aggregate diameter $d_{50} = 2.0$ mm). Figure 14 shows the grading curves for sand and gravel used for both mixes. 9 beams were made of sand concrete and 3 of gravel concrete. The uniaxial compression strength of beams measured on $10 \times 10 \times 10$ cm^3 cubic specimens was $f_c = 64 \pm 3$ MPa (sand concrete) and $f_c = 52 \pm 3$ MPa (gravel concrete).

In experiments, the usual digital camera Nikon 8400 ED (8MP) was applied with the image resolution of 3264×2448 pixels (Fig. 15a). The camera was mounted on a tripod with an additional frame to ensure a fully stable position. During

D=32cm
large: 32×128×4 cm, span 96 cm

D=16cm
medium:16×64×4 cm, span 48 cm
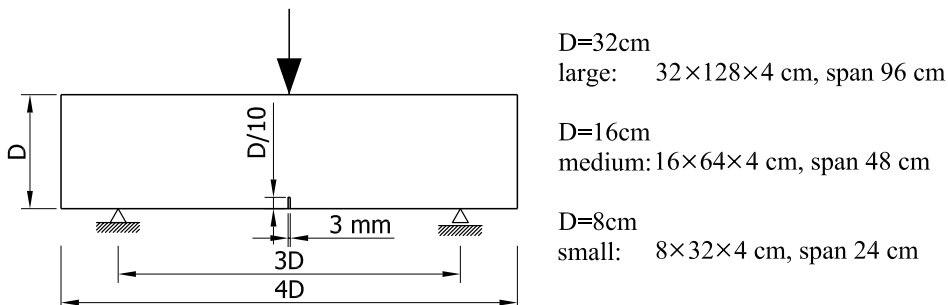
D=8cm
small: 8×32×4 cm, span 24 cm

Fig. 13. Geometry of concrete specimens subjected to three-point bending

Table 1. Contents of concrete mixes: a) with sand, b) with gravel

a)

No.	Material	Volume
1.	Sand	62%
2.	Cement	27%
3.	Water	11%

b)

No.	Material	Volume
1.	Gravel	76%
2.	Cement	17%
3.	Water	7%

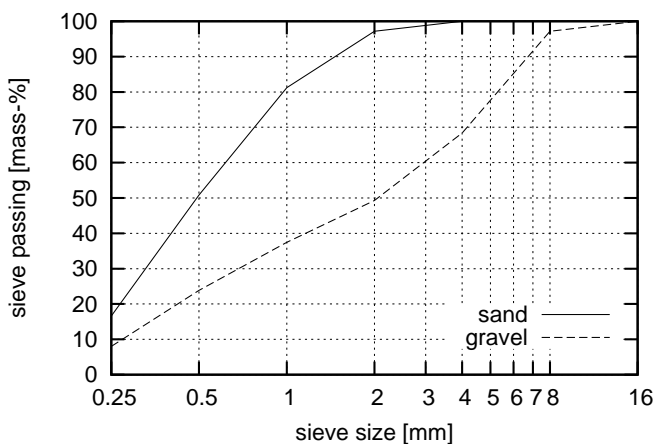**Fig. 14.** Grading curve for sand and gravel used for concrete

a)   b)
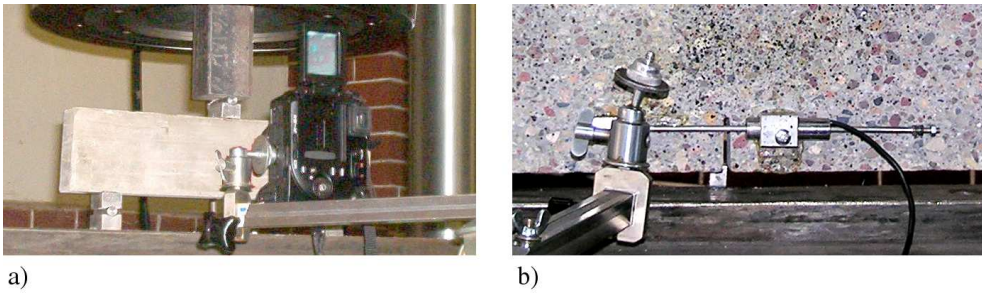
Fig. 15. Instrumentation used in the tests: a) Nikon 8400 digital camera, b) induction displacement gauge

experiments, load–deflection curves were registered and the fracture zone width was measured with an induction displacement gauge placed above the notch (Fig. 15b). First, the concrete beams were polished to achieve a smooth surface. Then, a random colour pattern was put on the surface, using two colour sprays: black and yellow. The images were shot once per minute.

5. Experimental Results

Figure 16 shows some beams after failure with a single crack propagated from the notch up to the top. The typical load–deflection curves for sand and gravel concrete beams are presented in Figures 17 and 18. In turn, Figure 19 shows the measured size effect for all experiments with sand concrete beams compared with the size effect law by Bazant (1984) and experimental results by Le Bellégo et al (2003). In the case of gravel concrete beams, due to only three performed tests, the measured size effect was not shown.

A pronounced size effect was observed in experiments (the larger the beam, the smaller the strength). The material ductility increased with decreasing beam size. The results are in satisfactory agreement with the size effect law (Bazant 1984) which is valid for structures with pre-existing notches or large cracks:

$$\sigma = \frac{B f_t}{\sqrt{1 + \dfrac{D}{D_0}}}, \tag{5}$$

where: σ – nominal strength, f_t – tensile strength, B – dimensionless geometry-dependent parameter which depends on the geometry of the structure and of the crack, D – specimen size and D_0 – size-dependent parameter called transitional size.

To find the parameters B and D_0 from FE-analysis, a nonlinear least-squares (NLLS) Marquardt-Levenberg algorithm was used. In spite of a small amount of sand concrete specimens (9), a satisfactory agreement with the Bazant's size effect
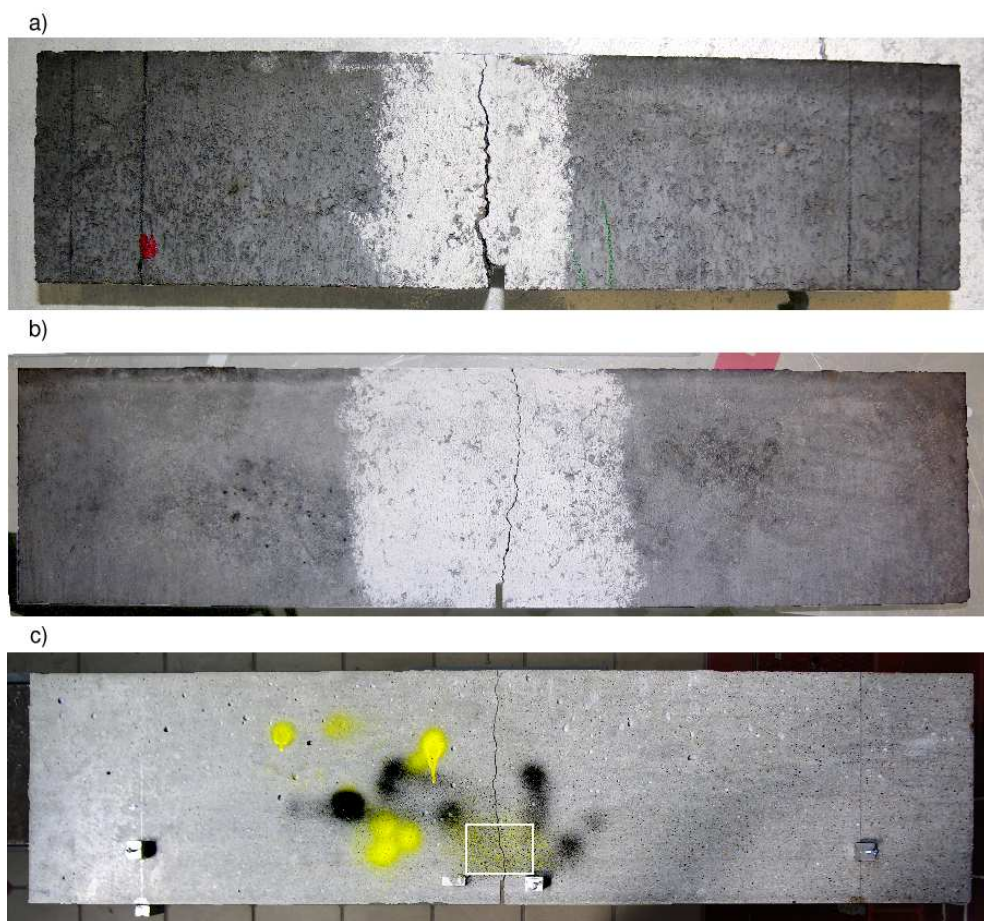
a)

b)

c)

Fig. 16. Beams after failure: a) small size beam (back side), b) medium size beam (back side), c) large size beam (front side with the black–yellow pattern inside of the image area marked by white rectangle)

law was achieved (Fig. 19a). The measured data match also the experimental results by Le Bellégo et al (2003) (Fig. 19b).

The displacement measured with the aid of the induction displacement gauge was used to verify the width of the fracture process zone obtained with DIC (Fig. 20). One assumed that the measured displacement was equal to the integral of strain over the width of the fracture process zone:

$$\Delta L = \int \varepsilon \, dl \approx \sum \varepsilon d, \tag{6}$$

where d is the distance between search patches expressed in millimeters in the DIC method. Before the beam failure, a perfect fit occurred between two curves, after the failure a small discrepancy took place.
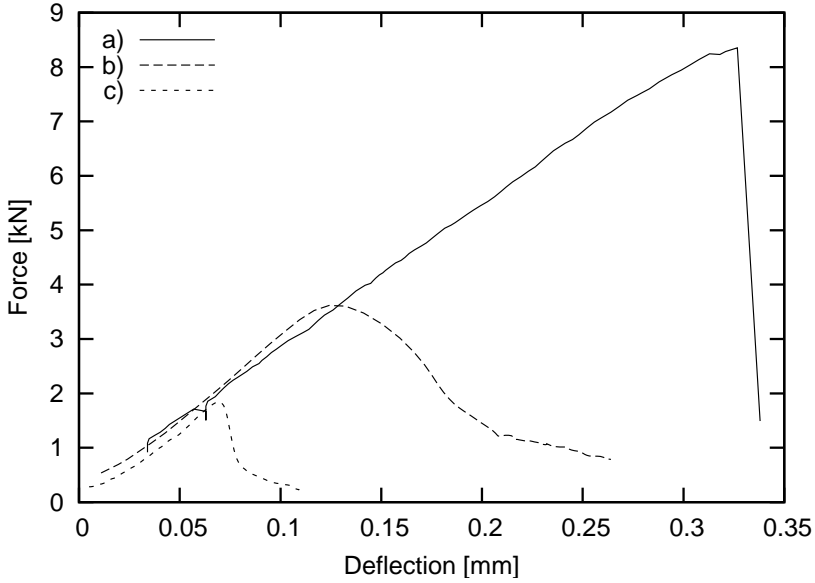
Fig. 17. Vertical force at mid–span versus beam deflection (sand concrete): a) large size beam, b) medium size beam, c) small size beam
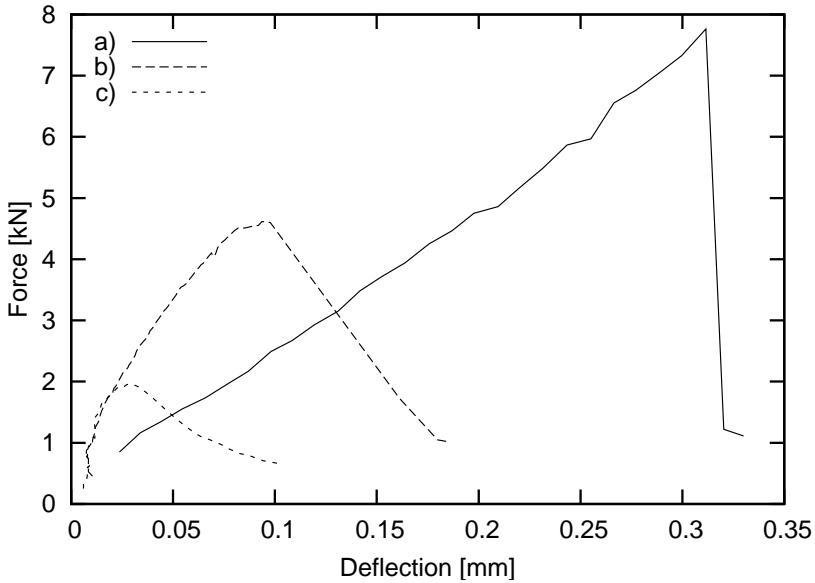

Fig. 18. Vertical force at mid–span versus beam deflection (gravel concrete): a) large size beam, b) medium size beam, c) small size beam
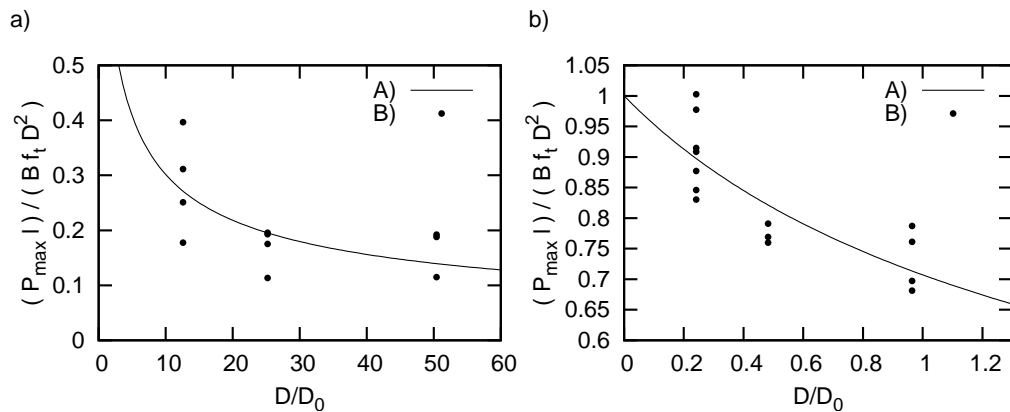
a)

b)

Fig. 19. Size effect in three-point bending tests (D is beam height, l is beam span, f_t is tensile strength, D_0 and B are parameters): a) experimental results with sand concrete (B) compared with the size effect law by Bazant (1984) with $D_0 = 0.0063$ and $B = 81.89$ (A), b) experimental results by Le Bellégo et al (2003) compared with the size effect law by Bazant (1984) with $D_0 = 0.332$ and $B = 23.93$ (A)
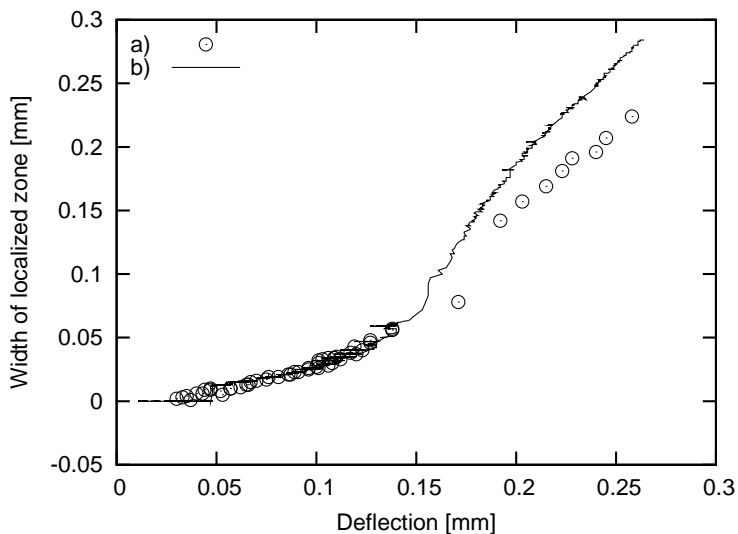

Fig. 20. Width of fracture zone in medium size beam (sand concrete) measured: a) by DIC, b) by induction displacement gauge (Eq. 6)
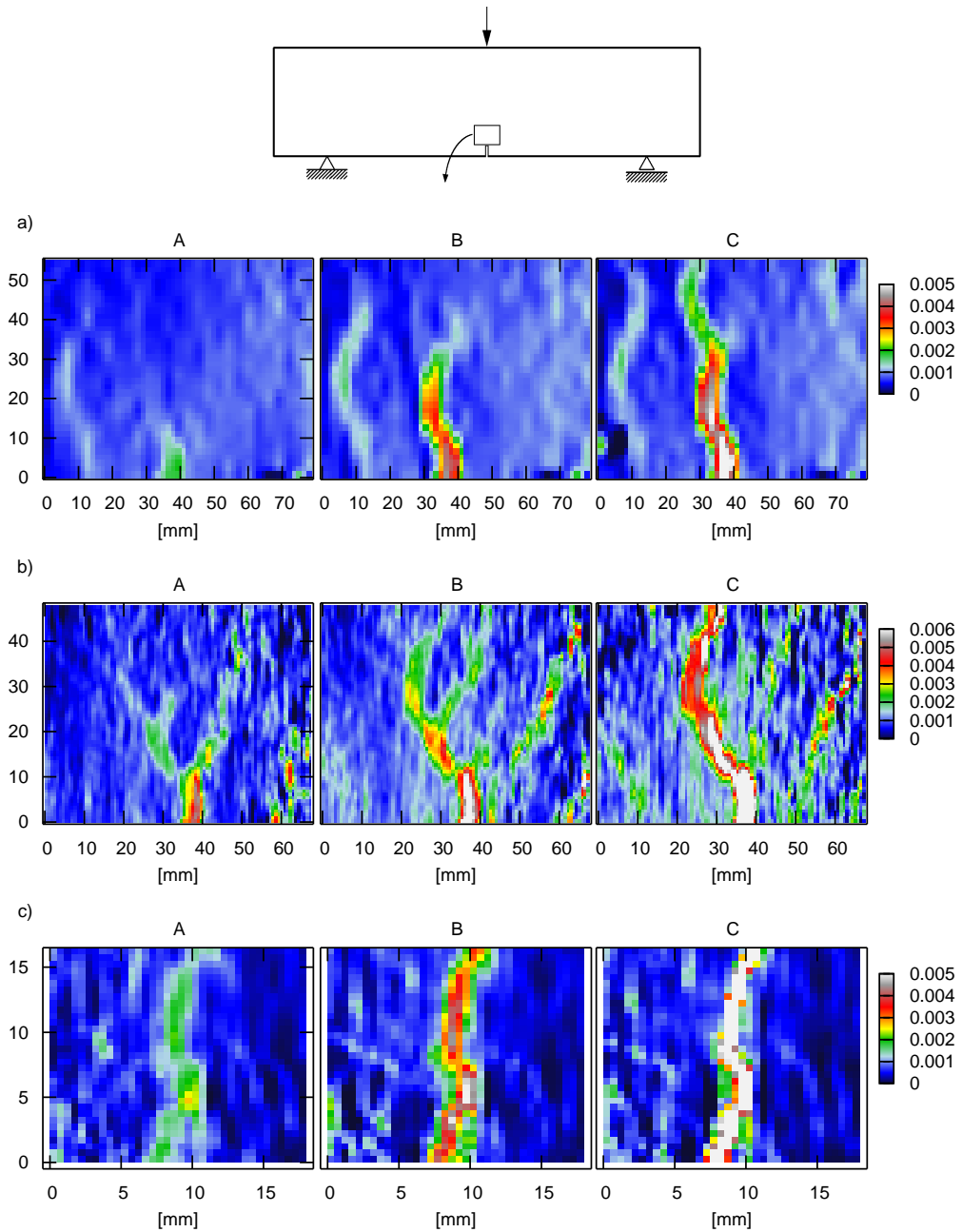
Fig. 21. Evolution of strain field during experiments from DIC (sand concrete): a) small size beam (search patch size is 200), b) medium size beam (search patch size is 210), c) large size beam (search patch size is 210), A) before the peak, B) at peak, C) after the peak
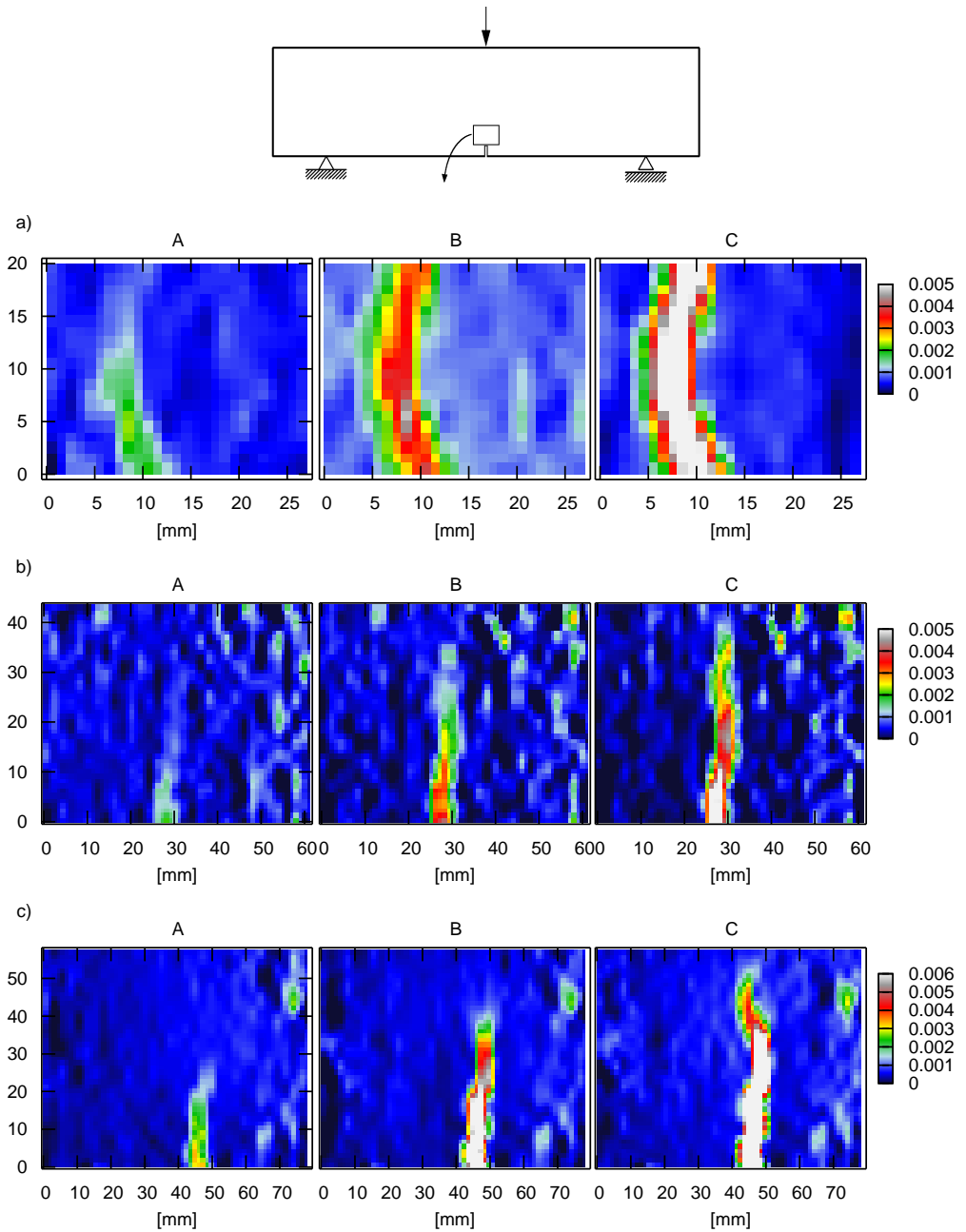
Fig. 22. Evolution of strain field during experiments from DIC (gravel concrete): a) small size beam (search patch size is 190), b) medium size beam (search patch 170), c) large size beam (search patch 170), A) before the beak, B) at peak, C) after the peak
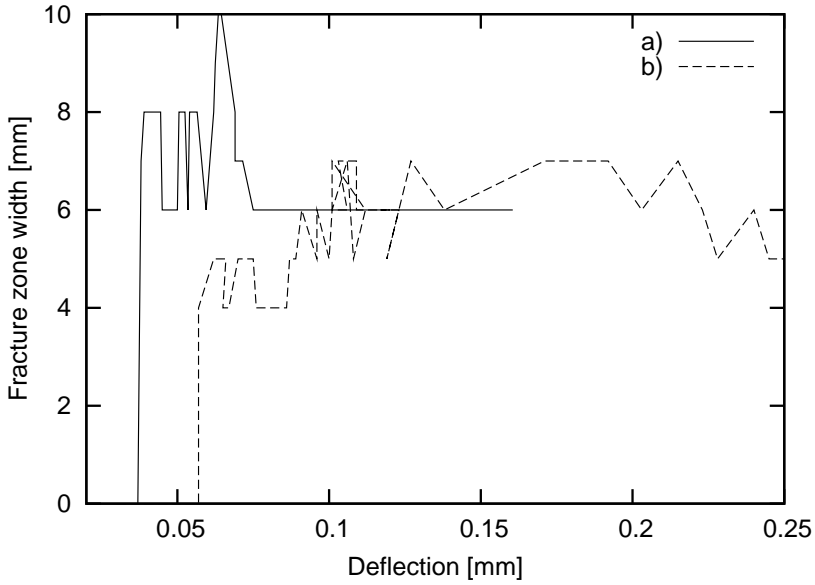
Fig. 23. Evolution of width of fracture process zone during experiments: a) medium size beam (gravel concrete), b) medium size beam (sand concrete)
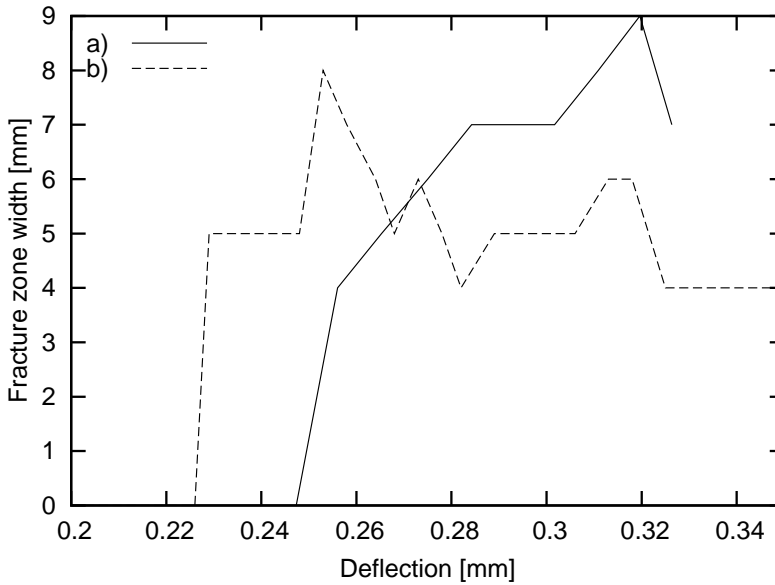

Fig. 24. Evolution of width of fracture zone during experiments: a) large size beam (gravel concrete), b) large size beam (sand concrete)

Figures 21 and 22 demonstrate the evolution of the horizontal strain in concrete beams from DIC. The fracture process zone occurs before the peak on the load–deflection diagram. The zone can be almost straight or it can be curved. In some cases, a pattern of localized fracture zones was created at the beginning of loading (Fig. 21b). The width of the fracture process zone was about 6 ± 1 mm ($12d_{50}$, $1.5d_a$) for sand concrete with $d_{50} = 0.5$ mm and $d_a = 4$ mm, and 7 ± 1 mm ($3.5d_{50}$, $0.5d_a$) for gravel concrete with $d_{50} = 2.0$ mm and $d_a = 16$ mm, before the failure. In general, the zone width (at the level of 5 mm above the notch) evolved during the beam loading (Figs. 23 and 24) (it mainly increased) which was in agreement with other experiments (Pijaudier-Cabot et al 2004). To obtain smoother curves, the zone width should be estimated as a mean value from different levels above the notch.

6. Conclusion

The model tests with notched concrete beams under three-point bending show that:

The Digital Image Correlation is a very effective and simple optical technique to determine the strain field on the surface of concrete with a large accuracy and without any physical contact. During the experiment, the digital camera must be fixed. Larger search patches increase accuracy and reduce noise, but also at the same time they blur the boundaries between regions with different strain.

A strong size effect occurs in concrete beams subject to bending. The beam ductility and nominal strength increase with decreasing specimen size.

The fracture process zone is created before the peak on the load–deflection diagram is reached. It can occur as a single zone or a pattern of zones at the beginning of deformation. The width of the fracture process zone increases during deformation and is equal to about 6–7 mm before the failure. The zone can be almost straight or strongly curved.

The currently used algorithm will be improved by taking into account all three colour channels from the image and by applying a Fast Fourier Transform method to accelerate the computation of the correlation function.

References

Bazant Z. P. (1984) Size effect in blunt fracture: concrete, rock, metal, *J. Engng. Mech. ASCE*, **110**, 518–535.

Bazant Z. P. (2003) *Scaling of Structural Strength*, Hermes-Penton, London.

Bazant Z. P., Jirasek M. (2002) Nonlocal integral formulations of plasticity and damage: survey of progress, *J. Engng. Mech.*, **128** (11), 1119–1149.

Bazant Z. P., Oh B. H. (1983) Crack band theory for fracture of concrete, *Material Structures, RILEM*, **16**, 155–177.

Bazant Z. P., Planas J. (1998) *Fracture and Size Effect in Concrete and other Quasi-brittle Materials*, CRC Press, Boca Raton.

Bhandari A. R., Inoue J. (2005) Experimental study of strain rates effects on strain localization characteristics of soft rocks, *Journal of the Mechanics and Physics of Solids*, **45** (1), 125–140.

Bobiński J., Tejchman J. (2006) Modeling of strain localization in quasi-brittle materials with a coupled elasto-plastic-damage model, *J. Theoretical and Applied Mechanics*, **4**, 44.

Dersch H. (1999) Testing Interpolator Quality, http://www.path.unimelb.edu.au/%7Edersch/interpolator/interpolator.html.

Eckert W., Nicholas J. M., Gray T., Hutter K. (2003) Particle Image Velocimetry for granular avalanches, *Lecture Notes in Applied and Computational Mechanics*: *Dynamic Response of Granular Materials under Large and Catastrophic Deformations* (eds. Hutter K., Kirchner N.), **11**, Springer, 195–219.

Ferrara I., di Prisco M. (2001) Mode and fracture behaviour in concrete: nonlocal damage modeling, *ASCE Journal of Engineering Mechanics*, **127** (7) 678–692.

Geers M., Peijs T., Brekelmans W., de Borst R. (1996) Experimental monitoring of strain localization and failure behaviour of composite materials, *Compos. Sci. Technol.*, **56**, 1283–1290.

Le Bellégo C., Dube J. F., Pijaudier-Cabot G., Gerard B. (2003) Calibration of nonlocal damage model from size effect tests, *European Journal of Mechanics A/Solids*, **22**, 33–46.

Mahnken R., Kuhl E. (1999) Parameter identification of gradient enhanced damage models, *European Journal of Mechanics A/Solids*, **18**, 819–835.

Michalowski R. R., Shi L. (2003) Deformation patterns of reinforced foundation sand at failure, *Journal of Geotechnical and Geoenvironmental Engineering*, **129** (6), 439–449.

Nübel K. (2002) *Experimental and Numerical Investigation of Shear Localization in Granular Materials*, Publication Series of the Institute of Soil and Rock Mechanics, University of Karlsruhe.

Pijaudier-Cabot G., Bazant Z. P. (1987) Nonlocal damage theory, *ASCE Journal of Engineering Mechanics*, **113**, 1512–1533.

Pijaudier-Cabot G., Haidar K., Dube J. F. (2004) Non-local damage model with evolving internal length, *Int. J. Num. and Anal. Meths. in Geomech.*, **28**, 633–652.

Raffel M., Willert C., Kompenhaus J. (1998) *Particle Image Velocimetry*, Springer, Berlin–Heidelberg.

Rechenmacher A. L. (2006) Grain-scale processes governing shear band initiation and evolution in sands, *Journal of the Mechanics and Physics of Solids*, **54**, 22–45.

Słomiński C., Niedostatkiewicz M., Tejchman J. (2006) Deformation measurements in granular bodies using a Particle Image Velocimetry technique, *Archives of Hydro-Engineering and Environmental Mechanics*, **53** (1), 71–94.

Słomiński C., Niedostatkiewicz M., Tejchman J. (2007) Application of particle image velocimetry (PIV) for deformation measurement during granular silo flow, *Powder Technology*, **173**, 1–18.

van Vliet M. R. A., van Mier J. G.. M. (1996) Experimental investigation of concrete fracture under uniaxial compression, *Mechanics of Cohesive-Frictional Materials*, **1**, 115–127.

White D. J., Take W. A., Bolton M. D. (2003) Soil deformation measurement using particle image velocimetry (PIV) and photogrammetry, *Géotechnique*, **53** (7), 619–631.